Ultrathin Black Phosphorus Nanosheets for Efficient Singlet Oxygen Generation

Hui Wang,[†,§] Xianzhu Yang,[‡,§] Wei Shao,[†] Shichuan Chen,[†] Junfeng Xie,[†] Xiaodong Zhang,*[,†] Jun Wang,[‡] and Yi Xie*[,†]

[†]Hefei National Laboratory for Physical Science at the Microscale, Collaborative Innovation Center of Chemistry for Energy Materials, University of Science and Technology of China, Hefei 230026, Anhui, P. R. China

[‡]School of Life Sciences, University of Science and Technology of China, Hefei 230027, Anhui, P. R. China

Ⓢ *Supporting Information*

ABSTRACT: Benefiting from its strong oxidizing properties, the singlet oxygen has garnered serious attentions in physical, chemical, as well as biological studies. However, the photosensitizers for the generation of singlet oxygen bear in low quantum yields, lack of long wavelength absorption band, poor biocompatibility, undegradable in living tissues, and so on. Here we first demonstrate the exfoliated black phosphorus nanosheets to be effective photosensitizers for the generation of singlet oxygen with a high quantum yield of about 0.91, rendering their attractive applications in catalysis and photodynamic therapy. Through in vitro and in vivo studies, the water dispersible black phosphorus nanosheets show notable cancer therapy ability. In addition, the photodegradable character of black phosphorus from element to biocompatible phosphorus oxides further highlights its therapeutic potential against cancer. This study will not only expand the breadth of study in black phosphorus but also offer an efficient catalyst and photodynamic therapy agent.
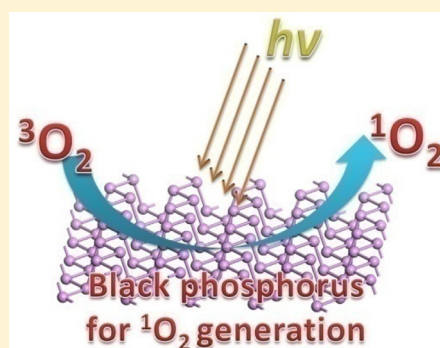
INTRODUCTION

Reactive oxygen species (ROS) are highly reactive ions and free radicals, including singlet oxygen ($^1O_2$), superoxide radicals ($O_2^{•-}$), hydrogen peroxide (H_2O_2), and hydroxyl radicals (•OH), among which the $^1O_2$ is the most prominent one.[1−3] Singlet oxygen has a relatively long lifetime, which can persist for over an hour in gas phase and $10^{−6}$−$10^{−3}$ second in solution.[3] As an excited state of molecular oxygen, the singlet oxygen is commonly generated via energy transfer from a photosensitizer to molecular oxygen under illumination, accompanied by the changed electronic configuration of O_2.[4,5] Because of its strong oxidizing ability, the $^1O_2$ has been studied in a wide range of applications from daily life to industrial production where the photooxidation catalysis and photodynamic therapy (PDT) are two of the most prominent applications.[6−9] Although singlet oxygen could be produced by many systems such as noble metals, heavy-atom-containing compounds as well as organic molecules, their applications are often limited by the poor water solubility, low quantum yield, easy photobleaching, and so on.[10−13] For practical applications, the materials should not only efficiently generate ROS but also be cost effective and biocompatible. In the past few years, the metal-free materials such as graphene and silicon were proposed for the generation of singlet oxygen,[5,8,9] whose applications in both catalysis and photodynamic therapy were preliminarily studied. However, because of the lacking of long wavelength absorption band and undegradable in living tissues, the further applications of carbon- and silicon-based materials were greatly restricted. In that case, new metal-free photosensitizer with broad light absorption, high singlet oxygen generation efficiency, as well as excellent biocompatibility is greatly demanded.[14,15]

Bearing this in mind, we paid our attention to the black phosphorus (B.P.), a metal-free layered semiconductor. As the most stable allotrope of elemental phosphorus, black phosphorus is constructed by puckered layers of phosphorus via weak van der Waals forces, which can be exfoliated into ultrathin two-dimensional (2D) nanosheets.[16,17] Different from graphene, black phosphorus is a semiconductor with thickness-dependent bandgap, which can be varied from about 0.3 eV for bulk to 2.0 eV for single layer,[18] indicating the broad absorption across the ultraviolet and entire visible light region. Very recently, the few-layer black phosphorus nanosheets have been highlighted as ideal platforms for the applications in electronic and optoelectronic devices for their impressive carrier mobility.[19,20] Considering the unique electronic structure of B.P., we expect that it may be a new metal-free semiconductor to generate singlet oxygen, which can be further applied in catalysis and PDT applications. However, the studies of B.P. mainly focus on its physical and transport properties, while rare efforts have been made to expand its application to other areas[21,22] such as chemical or biological fields.

Herein, for the first time, we highlight that black phosphorus, including bulk material and ultrathin nanosheets, are efficient photosensitizers for the generation of $^1O_2$ under the entire visible light region, suggesting their possible applications in catalysis and PDT. As expected, the ultrathin nanosheets of B.P. show dramatically enhanced ability for generating $^1O_2$ toward corresponding bulk counterpart. The as-obtained ultrathin black phosphorus nanosheets can oxidize double-bond containing reagents undergoing a Diels−Alder addition, exhibiting promising catalytic activities. In addition, in vitro and in vivo studies suggest that the ultrathin B.P. nanosheets are efficient photodynamic therapy agents for the treatment of cancer. The photodegradable character of B.P. from elemental phosphorus to biocompatible phosphorus oxides under light irradiation further heighten its possibility in clinical cancer therapy.

■ EXPERIMENTAL SECTION

Preparation of Bulk Black Phosphorus. Bulk black phosphorus was prepared through a facile low-pressure transport route according to the literature.[23] In detail, 500 mg of red phosphorus, 20 mg of tin, and 10 mg of SnI_4 were sealed in an evacuated Pyrex tube. The tube was heated at 923 K for 5 h with a heating ramp rate of about 1.35 K per min and then the temperature was reduced to 773 K with a cooling rate of 0.33 K per min, followed with a natural cooling process. The black product was then collected and washed with hot toluene and acetone for several times to remove the residual mineralizer. After being dried under vacuum, the product was kept in a glovebox for further analysis.

Preparation of Ultrathin Black Phosphorus Nanosheets. The ultrathin black phosphorus nanosheets were prepared by liquid exfoliation of corresponding bulk sample. In detail, 50 mg of the obtained bulk black phosphorus was dispersed in 100 mL of distilled water that bubbled with argon to eliminate the dissolved oxygen molecules for avoiding the oxidation, and the mixture solution was then sonicated in ice water for 8 h. Herein, the ice water was used to keep the system in a relatively low temperature. Afterward, the resultant brown suspension was centrifuged at 1500 rpm for 10 min to remove the residual unexfoliated particles and the supernatant was collected for further use.

Photodegradation of 1,3-Diphenylisobenzofuran (DPBF). Typically, 100 mL of ethanol solution with DPBF (20 μg/mL) and ultrathin B.P. nanosheets (10 μg/mL) were stirred in the dark for 100 min to reach the adsorption/desorption equilibrium prior to the test. A xenon lamp (PLS-SXE300/300UV, Trusttech Co., Ltd. Beijing) with a 600 nm long pass filter was used as the light source. The samples were taken at different times for UV−vis measurements. The measurements under various gas environments were performed with continuous gas bubbling. The concentration of NaN_3 for scavenger measurement was 50 μg/mL.

Photodynamic Killing of Cancer Cells. The in vitro cytotoxicity was assessed using a standard MTT (3-(4,5-dimethylthiazol-2-yl)-2,5-diphenyltetrazolium bromide) viability assay against MDA-MB-231 cells. Cells were seeded in 96-well plates at 10000 cells per well in 100 μL of complete Dulbecco's Modified Eagle Medium (DMEM) medium supplemented with 10% fetal bovine serum (FBS) and incubated at 37 °C in a 5% CO_2 atmosphere for 24 h. Then, 100 μL of ultrathin B.P. nanosheets in complete DMEM at different concentrations were used to replace the culture medium. After incubation at 37 °C for 4 h, cells were incubated with fresh media and irradiated by the 660 nm laser at the power density of 0.5 W cm^{-2} for 10 min. The cells were then incubated at 37 °C for additional 72 h before the MTT assay to determine the cell viabilities.

Intracellular ROS Assay. ROS generation inside cells under light irradiation was detected using DCF-DA Cellular Reactive Oxygen Species Assay Kit. MDA-MB-231 cells (1×10^5 cells/well) were seeded on coverslips on a 24-well plate and incubated for 24 h. The medium was replaced with complete DMEM medium containing ultrathin B.P. nanosheets as described above. After incubation for 4 h, DCF-DA was added according to the standard protocol provided by the suppliers. After 10 min incubation, cells were washed twice with PBS and irradiated by the 660 nm laser at the power density of 0.5 W cm^{-2} for 10 min. Then the medium was replaced with PBS and fluorescence images of treated cells were acquired under a Nikon TE2000-U inverted fluorescence microscope.

Cell Apoptosis Analysis. For the cell apoptosis analysis, MDA-MB-231 cells were seeded into 6-well plates (2×10^5 per well) and incubated for 24 h. Then, 100 μL of ultrathin B.P. nanosheets in complete DMEM (0.2 μg/mL) were used to replace the culture medium. After incubation at 37 °C for 4 h, cells were irradiated by the 660 nm laser as described above. Then the cells were further cultured 72 h, collected, stained by the annexin V-FITC apoptosis detection kit I (BD Biosciences, San Diego, CA), and detected by flow cytometry.

Xenograft Tumor Model. BALB/nu-nu nude mice (6 weeks old) were purchased from Vital River Laboratories (Beijing, China), and all animals received care in compliance with the guidelines outlined in the Guide for the Care and Use of Laboratory Animals. The procedures were approved by the University of Science and Technology of China's Animal Care and Use Committee. The xenograft tumor model was generated by injecting MDA-MB-231 cells (2×10^6 per mouse) in the mammary fat pad of each mouse. When the tumor volumes reached about 50 mm^3, the mice received a subcutaneous injection of 30 μL (500 μg/mL) of aqueous suspension of ultrathin B.P. nanosheets. The tumor site was irradiated by a 660 nm laser (0.5 W cm^{-2}) for 20 min at 12 h postinjection. Tumor growth was monitored by measuring the perpendicular diameter of the tumor using calipers. The estimated volume was calculated according to the following formula: tumor volume (mm^3) = 0.5 × length × width^2. At the last time point, the mice were sacrificed and the tumor tissue were excised and imaged.

Immunohistochemical Analysis. The tissues were fixed in 4% formaldehyde and embedded in paraffin for analysis. Paraffin-embedded 5 μm tumor sections were obtained for immunohistochemical staining of the proliferating cell nuclear antigen (PCNA) and the terminal transferase UTP nick-end labeling (TUNEL) assay.

Evaluation of the $^1O_2$ Quantum Yield by Detecting Its Emission. The $^1O_2$ emission signal at around 1270 nm was monitored by JY FLUOROLOG-3-TOU fluorescence with a near-infrared (NIR) detector, and the excitation wavelength was 530 nm. Rose Bengal (RB) was chosen to be the standard photosensitizer ($\Phi_{RB} = 0.86$, in ethanol).[24] The absorptions of the solution at 530 nm were adjusted to ~0.2 OD to eliminate the inner filter effect. The $^1O_2$ quantum yield of B.P. nanosheets was calculated by comparing the luminescence intensity toward that of Rose Bengal. In detail, $\Phi_{B.P.} = \Phi_{RB}(I_{B.P.}/I_{RB})$, where $I_{B.P.}$ and I_{RB} mean the PL peak areas of $^1O_2$ produced by B.P. nanosheets and RB, respectively.

Sample Characterizations. X-ray diffraction (XRD) were performed on a Philips X'Pert Pro Super diffractometer with Cu Kα radiation ($\lambda = 1.54178$ Å). Raman spectra were carried out on a LABRAM-HR confocal laser micro Raman spectrometer 750 K with 514 nm excitation at a laser power of 0.5 mW at room temperature. Transmission electron microscopy (TEM) images were taken on a JEOL-2010 transmission electron microscope with an acceleration voltage of 200 kV. High-angle annualar dark-field scanning transmission electron microscopy (HAADF-STEM) image, Electron energy loss spectroscopy (EELS) spectrum, energy dispersive spectrometry (EDS), and corresponding EDS mapping analysis were acquired on a JEM 2100F (field emission) transmission electron microscopes equipped with an Oxford INCA x-sight EDS Si(Li) detector at an acceleration voltage of 200 kV. X-ray photon spectroscopy (XPS) were acquired on an ESCALAB MK II with Mg Kα as the excitation source. Atomic force miscroscopy (AFM) measurement was performed by means of Veeco DI Nanoscope Multi Mode V system. Inductively coupled plasma (ICP) emission spectra were carried out on a PerkinElmer 40 Optima 7300DV ICP emission spectroscope. UV−vis absorption spectra were recorded on a PerkinElmer Lambda 950 UV−vis−NIR spectrophotometer. Electron spin resonance (ESR) measurements were performed using a Bruker EMX plus model spectrometer operating at X-band frequencies (9.4 GHz) at room temperature.

■ RESULTS AND DISCUSSION

In this study, bulk B.P. was prepared by a facile low-pressure transport route according to previous report (see Experimental Section).[23] The as-obtained sample can be indexed into the orthorhombic black phosphorus with the standard JCPDS card no. 73-1358 for cell parameters of a = 3.314 Å, b = 10.478 Å, and c = 4.376 Å (Supporting Information Figure S1). As schematically illustrated in Figure 1a, the bulk B.P. could be
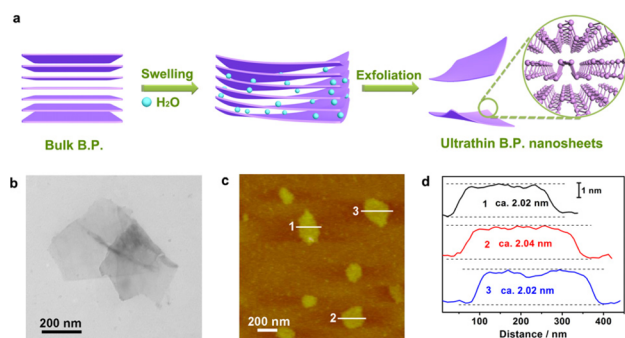

Figure 1. Preparation and morphology of ultrathin B.P. nanosheets. (a) Schematic illustration for the water exfoliation of bulk B.P. into ultrathin nanosheets. (b) TEM image. (c) AFM image. (d) Corresponding height image.

exfoliated into ultrathin nanosheets in water via a simple water exfoliation strategy.[25,26] Beyond water, other organic solvents such as *N*-methyl-2-pyrrolidone (NMP) can also exfoliate the bulk B.P. into ultrathin nanosheets with high exfoliation efficiency (Figure S3). We note that there were a few papers about liquid exfoliation of B.P. very recently, which mainly focused on exfoliating B.P. in organic solvents.[22,27−29] Although those organic solvents can efficiently exfoliate the bulk B.P., their adsorption on the surface of as-exfoliated nanosheets is too intimate to be removed. Herein, the ultrathin B.P. nanosheets with clean surface were obtained by exfoliating corresponding bulk sample in water with concentration of the nanosheets estimated to be ∼0.02 mg/mL. Figure 1b is the transmission electron microscopy (TEM) image of the as-exfoliated product, showing free-standing nanosheet with diameter of about several hundred nanometers. The thickness of the as-obtained nanosheet measured by atomic force microscopy (AFM) shows a height of about 2.0 nm (Figure 1c, 1d), which is consistent with about four individual B.P. layers.

Raman spectroscopy is an effective technique for sample identification by providing detailed vibrational and rotational modes. Herein, Raman spectra were performed to study the structural transformation of B.P. during the liquid exfoliation process. As shown in Figure 2a, the Raman spectra of bulk B.P. and exfoliated nanosheets show nearly identical peaks located at about 361, 438, and 466 cm^{-1}, which can be assigned to A_g^1, B_{2g}, and A_g^2 modes of B.P., respectively, indicating the exfoliated nanosheets maintain the structure of corresponding bulk counterpart. Compared with bulk B.P., the Raman spectrum of ultrathin B.P. nanosheets shows slightly shift toward high wavenumber, ascribing to the ultrathin thickness of the nanosheets as in previous reports.[30,31]

The structure of as-exfoliated nanosheets was further studied by the high-angle annular dark-field scanning transmission electron microscopy (HAADF-STEM), which is capable of resolving atomic structures with better than 2 Å lateral
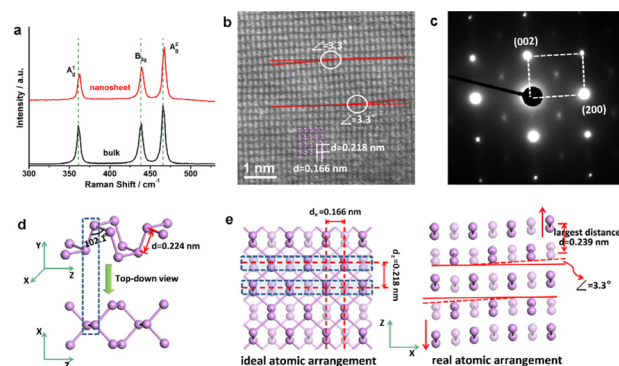

Figure 2. Structural characterizations of the ultrathin B.P. nanosheets. (a) Raman spectra of bulk B.P. and exfoliated B.P. nanosheets. (b) HAADF-STEM image of an exfoliated B.P. nanosheet. (c) The corresponding SAED pattern of (b). (d) Structure of B.P. projected along different directions. (e) Schematic illustration of the ideal and real atomic arrangement of the multilayered B.P. nanosheets.

resolution. The HAADF-STEM image in Figure 2b and corresponding selective area electron diffraction (SAED) pattern in Figure 2c reveal the as-exfoliated nanosheets to be single crystalline with [010] preferential orientation. As schematically illustrated in Figure 2d, because of the puckered structure of P layer in B.P., the nearby two P atoms overlayer with each other when projected along [010] direction, which cannot be distinguished in the HAADF-STEM image. In that case, each bright dot in the HAADF-STEM image of B.P. nanosheets as shown in Figure 2b represents the two overlayered P atoms. It is worth noting that the nearby bright dots in the HAADF-STEM image are not the atoms of the same puckered P layer for the multilayer thickness of the obtained nanosheets (Figure S4). The ideal distances between two nearby dots in the HAADF-STEM image of B.P. should be 0.166 and 0.218 nm for x and z directions, respectively. It is interesting that the dots in HAADF-STEM image for the exfoliated B.P. nanosheets deviate from their ideal sites, especially for the z-direction. In detail, as illustrated in Figure S5, the dots are upshifted or downshifted away from the ideal zero site, indicating parts of the P atoms in the exfoliated nanosheets are closely or loosely packed. As analyzed in Figure 2b, parts of the dots deviated from their ideal sites with gradually increased or decreased distance, showing an angle of about 3.3°, and the largest distance for z-direction is extended from 0.218 to 0.239 nm, which is 9.6% larger than that of ideal B.P. structure. At the same time, the shortest distance between two dots is estimated to be 0.207 nm, with 5.04% shortened to 0.218 nm. As is known, there were no perfect two-dimensional (2D) crystals, and the atomic arrangement of 2D crystals must undergo a certain degree of distortion to stabilize their unique structures.[32] In this study, the observation of atomic arranging fluctuation in the HAADF-STEM image gives the most direct evidence that there was structural disorder in the exfoliated B.P. nanosheets, which is just the reason for the stabilization of unique 2D structure of B.P.[33,34] Both the energy dispersive spectrum (EDS) and mapping analyses (Figure S6) reveal the presence and homogeneous distribution of P element in the sample, indicating the high purity of the nanosheets. The weak peak located at about 134 eV in X-ray photoelectron spectra (XPS) of the exfoliated B.P. nanosheets is the signal of P$_x$O$_y$, indicating the minor degradation on the surface of the nanosheets (Figure S7). Electron energy loss spectroscopy

(EELS) analysis (Figure S8) performed on an isolated nanosheet further confirmed its high purity. Those results clearly showed that the B.P. nanosheets with ultrathin thickness and structural disorder were successfully obtained by simple water exfoliation.

Previously, the atomically thin B.P. nanosheets were obtained by Scotch tape exfoliation, which are not stable and would be partially oxidized into phosphorus oxides in the copresence of water, oxygen, and light.[30] In that case, it is essential for us to explore the stability of our liquid-exfoliated nanosheets, especially for the nanosheets dispersed in water. To study this issue, the time-dependent XPS and Raman analyses were carried out to investigate the structure and composition of the as-exfoliated nanosheets in water for different times. As seen from Figures S9−S11, the exfoliated nanosheets can be stable in water for more than 2 weeks without obvious degradation in dark and preserve their nanosheet morphology, and the nanosheets dispersed in organic solvents would be more stable than that in water, for example, the exfoliated B.P. nanosheets can be stably dispersed in NMP for more than one month. We assumed that, different from Scotch tape exfoliation technique, during liquid exfoliation the solvent molecules would adsorb on the surfaces of as-exfoliated nanosheets to protect their against further oxidation and stable dispersion in the solvent. In addition, the solvents can further isolate the as-dispersed nanosheets from air and dramatically slow down the degradation process. The good stability of the B.P. nanosheets in water enables us to pursue their potential biological applications. It is interesting that the metal-free B.P. nanosheets have little effect on the cell viability even with high concentrations, indicating their low cytotoxicity and excellent biocompatibility (Figure S12).

Despite the stable dispersion of the ultrathin B.P. nanosheets in water, long-time light irradiation would dramatically accelerate the degradation of B.P. in water. As illustrated in Figure S13 and corresponding inductively coupled plasma atomic emission spectroscopy analysis (ICP-AES; Table S1), the fresh B.P. nanosheets would be almost fully degraded to phosphite ion, phosphate ion, or other P_xO_y species under intermittent light irradiation in water, among which the phosphite ion is the main degradation product of B.P. The light-induced degradation of ultrathin B.P. nanosheets in water further highlights their application in biological areas, as they can be readily degraded into biocompatible ions without any residual.

Although the bandgap of B.P. would enlarge after exfoliation into ultrathin nanosheets, the as-exfoliated nanosheets also show a broad light absorption across the entire visible light regions and extend to near-infrared regions (Figure S15). As a narrow bandgap semiconductor, we expect that the ultrathin B.P. nanosheets as well as bulk B.P. may generate singlet oxygen under light irradiation. It is known that the photogenerating ability of singlet oxygen could be evaluated by probe molecule under specific reactions, for example, the 1,3-diphenylisobenzofuran (DPBF) can react with $^1O_2$ undergoing a Diels−Alder 1,4-cycloaddition, showing a decrease of the absorption intensity at about 410 nm. Herein, for the first time, the singlet oxygen generation of B.P. was studied by using DPBF as the probe molecule in ethanol. As shown in Figure 3a and Figure S17, the absorption intensities around 410 nm for both of the bulk B.P. and ultrathin B.P. nanosheets were gradually decreased with the increasing of light irradiation time in air ($\lambda \geq 600$ nm, Xe lamp with 600 nm cutoff filter),
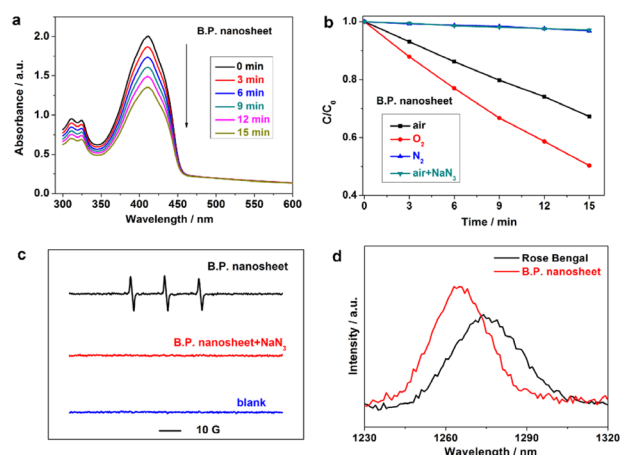

Figure 3. Singlet oxygen characterization. (a) Time-dependent absorption spectra of the DPBF with B.P. nanosheets in air. (b) Normalized absorbance of the DPBF in the presence of B.P. nanosheets in different conditions. (c) ESR spectra of B.P. nanosheets in the presence of TEMP in different conditions. Both the decomposing of DPBF and ESR spectra were carried out under Xe lamp with 600 nm cutoff filter. (d) $^1O_2$ emission at ~1270 nm induced by the commercial Rose Bengal and B.P. nanosheets in ethanol under excitation with a 530 nm light.

indicating the decomposing of DPBF, and the ultrathin B.P. nanosheets exhibit enhanced catalytic activity toward bulk B.P. To confirm that the reaction was induced by the generated $^1O_2$, a quantitative amount of sodium azide (NaN$_3$), a scavenger that can consume the generated $^1O_2$, was added with ultrathin B.P. nanosheets during the test. As displayed in Figure 3b, after adding NaN$_3$, the absorption of DPBF showed negligible change even after light irradiation for 15 min, indicating the active species generated by B.P. is singlet oxygen. Furthermore, to exclude the possible direct reaction between DPBF and photoexcited B.P. nanosheets, the photolysis of DPBF was carried out under continuous O$_2$/N$_2$ purge, respectively. The absorption of DPBF nearly unchanged under N$_2$ conditions, while dramatically decreased under O$_2$. The oxygen content-dependent character clearly indicates that the $^1O_2$ is generated under photosensitizing process by energy transfer from B.P. to ground-state oxygen.

The catalytic activity of B.P. was further examined by its ability for the photodecomposing of organic dyes in water such as methyl orange (MO). As seen from Figure S16, the ultrathin B.P. nanosheets display high catalytic activity, which need only 20 min for the degradation of 90% of MO molecules under visible light ($\lambda \geq 600$ nm). However, no obvious decomposing of MO can be detected when NaN$_3$ added with the ultrathin B.P. nanosheets, indicating this reaction was based on the photogenerated $^1O_2$. Although the ultrathin B.P. nanosheets show high reactivity in water, the light induced degradation of B.P. is a crucial handicap for its catalytic activity, which need further modification before meeting the standard for industry applications.

Electron spin resonance (ESR) spectrum is considered as the most direct evidence to identify the species of generated ROS. To further confirm the generation of singlet oxygen by B.P., we have employed the 2,2,6,6-tetramethylpiperidine (TEMP) as the $^1O_2$ trapping agent to examine the system by ESR technique under light irradiation ($\lambda \geq 600$ nm). As shown in Figure 3c and Figure S18, the ESR signals for the ultrathin B.P. nanosheets and bulk B.P. clearly display 1:1:1 triplet signal

characteristic with *g*-value of 2.0056 and hyperfine splitting constant (aN = 1.608 mT), which are consistent with those for 2,2,6,6-tetramethylpiperidine-*N*-oxyl (TEMPO). The results confirm that $^1O_2$ is produced by B.P. Although both the ultrathin B.P. nanosheets and bulk B.P. can induce the formation of $^1O_2$, the signal intensity of TEMPO in the case of ultrathin nanosheets is significantly higher than that of corresponding bulk. The dramatic enhancement of the singlet oxygen generation would attribute to the ultrathin character of the nanosheets, which not only provides rich surface atoms serving as the active sites but also reduces the electron−hole recombination rate. Besides, the much higher charge-carried mobility of the ultrathin B.P. nanosheets toward that of corresponding bulk sample[17] would also benefit for the singlet oxygen generation. The other trapping agent, such as 5,5-dimethyl-1-pyrroline-*N*-oxide (DMPO), was also used to exclude the possible generation of other ROS by B.P. No signal can be detected when added DMPO in ultrathin B.P. nanosheets, indicating neither $O_2^{\bullet-}$ nor •OH was generated by B.P. under visible light irradiation (Figure S18).

As is known, singlet oxygen can undergo radiative decay around 1270 nm, and the near-infrared emission was commonly used for determining quantum yields in solution.[35] Herein, by taking Rose Bengal (RB) as a standard photosensitizer, the $^1O_2$ quantum yield of ultrathin B.P. nanosheets was evaluated by the formula $\Phi_{B.P.} = \Phi_{RB}(I_{B.P.}/I_{RB})$. According to Figure 3d, the integral areas of $^1O_2$ luminescence produced by B.P. nanosheets and RB are about 645666 and 610180, respectively and based on the value for $\Phi_{RB} = 0.86$ in ethanol (Figure 3d), $\Phi_{B.P.}$ is estimated to be 0.91, which is higher than those of most reported photosentizers.[24] The slightly shift of $^1O_2$ spectrum between B.P. nanosheets and RB as shown in Figure 3d may derive from their various surface environments, which is a common phenomenon in luminescence.[36,37]

Benefiting from their good biocompatibility and high singlet oxygen generation, the water-dispersible B.P. nanosheets can be used for photodynamic therapy. The in vitro PDT efficiency and cytotoxicity of the B.P. nanosheets against cancer cells were quantitatively evaluated by a standard MTT (3-{4,5-dimethylthiazol-2-yl}-2,5-diphenyltetrazolium bromide, Invitrogen, USA) viability assay. As shown in Figure 4a, the ultrathin B.P. nanosheets have little effect on the cell viability in the dark, while the cell viability was gradually weakened with the increasing concentration of ultrathin B.P. nanosheets under light irradiation. In detail, after incubation with human MDA-MB-231 breast cancer cells for 4 h followed by irradiation (660 nm, 1 W cm^{-2}, 10 min), the ultrathin B.P. nanosheets exhibited significant cell growth inhibition, within IC$_{50}$ of 0.09 µg/mL. To investigate the mechanism of tumor cell growth inhibition, we detected intracellular ROS production by ultrathin B.P. nanosheets inside the cancer cells under irradiation with light by using a cell permeable fluorescent dye dichlorofluorescein (DCF). As shown in Figure 4b, incubation of ultrathin B.P. nanosheets without light irradiation exhibited very minimal fluorescence of DCF, while strong green fluorescence was observed in cells after irradiation with light, indicating the generation of ROS inside the cells during irradiation with light. Because the ultrathin B.P. nanosheets only generate singlet oxygen under visible light irradiation, herein the green fluorescence would be mainly induced by singlet oxygen. It should be noted that the inhibition of tumor cell growth was not caused by the photothermal effect because the temperature of the B.P. nanosheets suspension remained almost unchanged
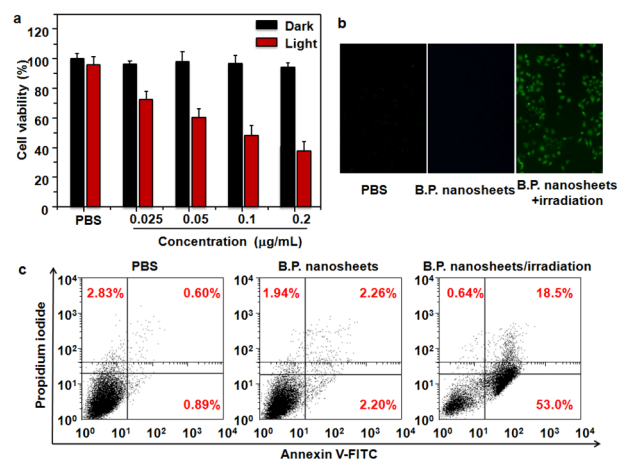

Figure 4. In vitro photodynamic therapy. (a) Cell viability with different concentrations of ultrathin B.P. nanosheets. (b) Oxidized DCF fluorescence in cell with different formulation. (c) Cell apoptosis following transfection with different formulations. Early apoptotic cells are shown in the lower right quadrant, and late apoptotic cells are shown in the upper right quadrant.

after irradiation, even at a higher concentration (1.0 µg/mL) (Figure S19). Furthermore, the intracellular singlet oxygen production by ultrathin B.P. nanosheets under light irradiation would induce cell apoptosis, which were analyzed by annexin V-FITC/PI staining. As shown in Figure 4c, the percentage of cells suffering apoptosis after irradiation with light was 71.5%. On the contrary, treatment of MDA-MB-231 cells without irradiation did not induce remarkable apoptosis when compared with PBS group. Therefore, on the basis of these results, it can be confirmed that the intracellular ROS could be produced by ultrathin B.P. nanosheets inside the cancer cells under light irradiation, which further induce cell apoptosis and inhibit cell proliferation.

To further reveal the potential of as-exfoliated ultrathin B.P. nanosheets for in vivo PDT in cancer therapy, we establish MDA-MB-231 breast tumors in situ in Balb/c nude mice. After the average tumor volume exceeded 60 mm^3, 15 mice were randomly divided into three groups, and each mouse was injected with 30.0 µL of the suspension of ultrathin B.P. nanosheets (500 µg/mL) or saline. For the PDT group, mice were exposed to the 660 nm laser for 20 min at the power density of 0.5 W/cm^2 after 12 h of intratumoral injection. The tumor growth was significantly hindered after being injected with ultrathin B.P. nanosheets and exposed to the light (Figure 5a). In contrast, treatment of tumor-bearing mice with B.P. nanosheets without irradiation could not inhibit tumor growth in comparison with PBS-treated mice. As expected, after treatment with ultrathin B.P. nanosheets under irradiation, the volume of the tumor was minimum (Figure 5b). Moreover, cell proliferation and apoptosis in the tumor tissues were analyzed by immunohistochemical staining after the treatment. As shown in Figure 5c, treatment with B.P. nanosheets under irradiation was demonstrated to be the most effective formulation in reducing the percentage of proliferating PCNA-positive tumor cells and increasing TUNEL-positive tumor cells, indicating therapeutic potential of ultrathin B.P. nanosheets for cancer therapy.
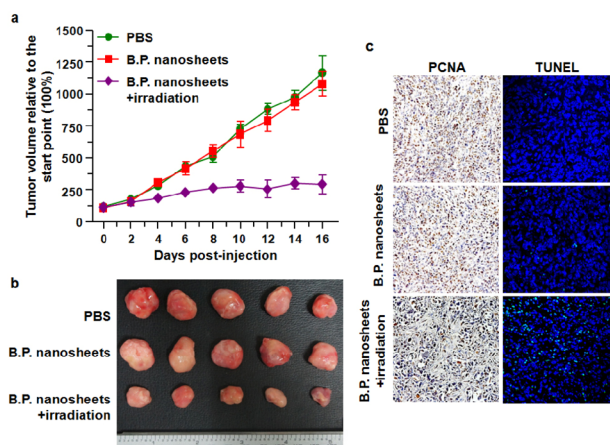
Figure 5. In vivo photodynamic therapy. (a) Time-dependent tumor growth in a murine tumor model after treatments with different formulations. (b) Imaging of tumors after treated with various formulations. (c) PCNA and TUNEL analysis of tumor tissues after treatment with various formulations. PCNA-positive proliferating cells are stained brown and TUNEL-positive apoptotic cells are stained green.

CONCLUSION

In conclusion, we have for the first time demonstrated the ultrathin B.P. nanosheets are efficient photosensitizers for the generation of singlet oxygen under the entire visible light region with a high quantum yield of about 0.91, which is higher than those of most reported PDT agents, and the water-exfoliated B.P. nanosheets could not only be stable in water for a long time but also retain their high singlet oxygen generation ability, rendering their applications in catalysis and photodynamic therapy. It is interesting that the structural disorder of ultrathin B.P. nanosheets was directly observed in the fluctuation of corresponding HAADF-STEM image, guaranteeing the stability of as-exfoliated nanosheets. In catalysis tests, the B.P. nanosheets show excellent photodegradation of organic components such as DPBF and MO. Through in vitro and in vivo studies, the B.P. nanosheets exhibit notable cell/tumor growth inhibition with small amount and short light irradiation time. Compared with other metal-free PDT agents, the B.P. nanosheets could be readily degradation into biocompatible phosphorus oxides under light irradiation without any residual, which further highlights its therapeutic potential for cancer treatment. We believe that this study can provide a new insight into the extensively studied black phosphorus.

ASSOCIATED CONTENT

Ⓢ Supporting Information

The Supporting Information is available free of charge on the ACS Publications website at DOI: 10.1021/jacs.5b06025.

> Supplementary characterizations, analysis of the purity, stability, photodegradation, and catalysis study of B.P. nanosheets (PDF)

AUTHOR INFORMATION

Corresponding Authors
*zhxid@ustc.edu.cn (X.Z.)
*yxie@ustc.edu.cn (Y.X.)
Author Contributions
§H.W. and X.Y. contributed equally.

REFERENCES

(1) Apel, K.; Hirt, H. *Annu. Rev. Plant Biol.* **2004**, *55*, 373.
(2) DeRosa, M. C.; Crutchley, R. J. *Coord. Chem. Rev.* **2002**, *233–234*, 351.
(3) Kearns, D. R. *Chem. Rev.* **1971**, *71*, 395.
(4) Schweitzer, C.; Schmidt, R. *Chem. Rev.* **2003**, *103*, 1685.
(5) Kovalev, D.; Fujii, M. *Adv. Mater.* **2005**, *17*, 2531.
(6) Montagnon, T.; Tofi, M.; Vassilikogiannakis, G. *Acc. Chem. Res.* **2008**, *41*, 1001.
(7) Dolmans, D. E. J. G. J.; Fukumura, D.; Jain, R. K. *Nat. Rev. Cancer* **2003**, *3*, 380.
(8) Ge, J.; Lan, M.; Zhou, B.; Liu, W.; Guo, L.; Wang, H.; Jia, Q.; Niu, G.; Huang, X.; Zhou, H.; Meng, X.; Wang, P.; Lee, C.-S.; Zhang, W.; Han, X. *Nat. Commun.* **2014**, *5*, 4596.
(9) Idris, N. M.; Gnanasammandhan, M. K.; Zhang, J.; Ho, P. C.; Mahendran, R.; Zhang, Y. *Nat. Med.* **2012**, *18*, 1580.
(10) Long, R.; Mao, K.; Ye, X.; Yan, W.; Huang, Y.; Wang, J.; Fu, Y.; Wang, X.; Wu, X.; Xie, Y.; Xiong, Y. *J. Am. Chem. Soc.* **2013**, *135*, 3200.
(11) Samia, A. C. S.; Chen, X.; Burda, C. *J. Am. Chem. Soc.* **2003**, *125*, 15736.
(12) Hou, L.; Zhang, X.; Pijper, T. C.; Browne, W. R.; Feringa, B. L. *J. Am. Chem. Soc.* **2014**, *136*, 910.
(13) Xiao, L.; Gu, L.; Howell, S. B.; Sailor, M. *ACS Nano* **2011**, *5*, 3651.
(14) Garner, A.; Wilkinson, F. *Chem. Phys. Lett.* **1977**, *45*, 432.
(15) Abdel-Shafi, A. A.; Wilkinson, F. *J. Phys. Chem. A* **2000**, *104*, 5747.
(16) Morita, A. *Appl. Phys. A: Solids Surf.* **1986**, *39*, 227.
(17) Li, L.; Yu, Y.; Ye, G. J.; Ge, Q.; Ou, X.; Wu, H.; Feng, D.; Chen, X. H.; Zhang, Y. *Nat. Nanotechnol.* **2014**, *9*, 372.
(18) Tran, V.; Soklaski, R.; Liang, Y.; Yang, L. *Phys. Rev. B: Condens. Matter Mater. Phys.* **2014**, *89*, 235319.
(19) Liu, H.; Du, Y.; Deng, Y.; Ye, P. D. *Chem. Soc. Rev.* **2015**, *44*, 2732.
(20) Xia, F.; Wang, H.; Jia, Y. *Nat. Commun.* **2014**, *5*, 4458.
(21) Park, C. M.; Sohn, H. J. *Adv. Mater.* **2007**, *19*, 2465.
(22) Hanlon D.; Backes, C.; Doherty E.; Cucinotta C.; Berner N.; Boland C.; Lee K.; Lynch P.; Gholamvand Z.; Harvey A.; Zhang S.; Wang K.; Moynihan G.; Pokle A.; Ramasse Q.; McEvoy N.; Blau W.; Wang J.; Sanvito S.; ORegan D.; Duesberg G.; Nicolosi V.; Coleman J. *cond-mat.mes-hall*, **2015**, arXiv:1501.01881.
(23) Stan, M. C.; Zamory, J. v.; Passerini, S.; Nilges, T.; Winter, M. *J. Mater. Chem. A* **2013**, *1*, 5293.
(24) Redmond, R. W.; Gamlin, J. N. *Photochem. Photobiol.* **1999**, *70*, 391.
(25) Coleman, J. N.; Lotya, M.; O'Neill, A.; Bergin, S. D.; King, P. J.; Khan, U.; Young, K.; Gaucher, A.; De, S.; Smith, R. J.; Shvets, I. V.; Arora, S. K.; Stanton, G.; Kim, H.-Y.; Lee, K.; Kim, G. T.; Duesberg, G. S.; Hallam, T.; Boland, J. J.; Wang, J. J.; Donegan, J. F.; Grunlan, J. C.; Moriarty, G.; Shmeliov, A.; Nicholls, R. J.; Perkins, J. M.; Grieveson, E. M.; Theuwissen, K.; McComb, D. W.; Nellist, P. D.; Nicolosi, V. *Science* **2011**, *331*, 568.
(26) Zhang, X.; Xie, X.; Wang, H.; Zhang, J.; Pan, B.; Xie, Y. *J. Am. Chem. Soc.* **2013**, *135*, 18.
(27) Brent, J. R.; Savjani, N.; Lewis, E. A.; Haigh, S. J.; Lewis, D. J.; O'Brien, P. *Chem. Commun.* **2014**, *50*, 13338.

(28) Yasaei, P.; Kumar, B.; Foroozan, T.; Wang, C.; Asadi, M.; Tuschel, D.; Indacochea, J. E.; Klie, R. F.; Salehi-Khojin, A. *Adv. Mater.* **2015**, *27*, 1887.

(29) Kang, J.; Wood, J. D.; Wells, S. A.; Lee, J.-H.; Liu, X.; Chen, K.-S.; Hersam, M. C. *ACS Nano* **2015**, *9*, 3596.

(30) Favron, A.; Gaufres, E.; Fossard, F.; Phaneuf-L'Heureux, A.-L.; Tang, N. Y. W.; Levesque, P. L.; Loiseau, A.; Leonelli, R.; Francoeur, S.; Martel, R. *Nat. Mater.* **2015**, *14*, 826.

(31) Zhang, X.; Xie, H.; Liu, Z.; Tan, C.; Luo, Z.; Li, H.; Lin, J.; Sun, L.; Chen, W.; Xu, Z.; Xie, L.; Huang, W.; Zhang, H. *Angew. Chem., Int. Ed.* **2015**, *54*, 3653.

(32) Meyer, J. C.; Geim, A. K.; Katsnelson, M. I.; Novoselov, K. S.; Booth, T. J.; Roth, S. *Nature* **2007**, *446*, 60.

(33) Fasolino, A.; Los, J. H.; Katsnelson, M. I. *Nat. Mater.* **2007**, *6*, 858.

(34) Zhang, X.; Zhang, J.; Zhao, J.; Pan, B.; Kong, M.; Chen, J.; Xie, Y. *J. Am. Chem. Soc.* **2012**, *134*, 11908.

(35) Niedre, M.; Patterson, M. S.; Wilson, B. C. *Photochem. Photobiol.* **2002**, *75*, 382−391.

(36) Kořinek, M.; Dědic, R.; Svoboda, A.; Hála, J. *J. Fluoresc.* **2004**, *14*, 71.

(37) Bilski, P.; Zhao, B.; Chignell, C. F. *Chem. Phys. Lett.* **2008**, *458*, 157.